



Bismuth-rich strategy induced photocatalytic molecular oxygen activation properties of bismuth oxyhalogen: The case of $\text{Bi}_{24}\text{O}_{31}\text{Cl}_{10}$

Xiaoli Jin^a, Liqun Ye^{a,*}, Hui Wang^b, Yurong Su^a, Haiquan Xie^{a,*}, Zhiguo Zhong^a, He Zhang^a

^a College of Chemistry and Pharmaceutical Engineering, Nanyang Normal University, Nanyang 473061, People's Republic of China

^b CAS Key Laboratory of Nuclear Radiation and Nuclear Energy Techniques, and Multidisciplinary Initiative Center, Institute of High Energy Physics, Chinese Academy of Sciences, Beijing 100049, People's Republic of China

ARTICLE INFO

Article history:

Received 23 July 2014

Received in revised form 21 October 2014

Accepted 29 October 2014

Available online 4 November 2014

Keywords:

$\text{Bi}_{24}\text{O}_{31}\text{Cl}_{10}$

Molecular oxygen activation

Photocatalysis

Bismuth-rich strategy

ABSTRACT

Molecular oxygen activation is very important for photocatalytic degradation of organic pollutants. In this paper, $\text{Bi}_{24}\text{O}_{31}\text{Cl}_{10}$ nanosheets with {100} facets exposure were successfully synthesized by hydromel method and characterized. The size of a single nanosheet is about 5 μm in width and 10–30 nm in thickness, which results in a large ratio of surface to thickness and higher exposure ratio of {100} facets. The Mott–Schottky test revealed that the conduction band minimum (CBM) of $\text{Bi}_{24}\text{O}_{31}\text{Cl}_{10}$ is more negative than BiOCl due to the bismuth-rich strategy. And the photocatalytic results showed that as-synthesized $\text{Bi}_{24}\text{O}_{31}\text{Cl}_{10}$ showed higher photocatalytic properties than BiOCl for activate molecular oxygen to generate superoxide radical ($\text{O}_2^{\bullet-}$) under visible light ($\lambda > 420\text{ nm}$) irradiation, and generate hydroxyl radical ($\bullet\text{OH}$) under UV–vis light irradiation. This strategy in this work may potentially be extended to other bismuth-based photocatalysts for molecular oxygen activation.

© 2014 Elsevier B.V. All rights reserved.

1. Introduction

Photocatalysis technology has been studied widely since the photocatalytic splitting of water by TiO_2 electrodes was discovered in 1970s [1]. Due to its potential applications in environmental pollution purification and energy conversion, semiconductor photocatalysis technology has been considered as a green technology to completely eliminate the organic pollutants in an environmentally friendly manner [2–11]. There is no doubt that the photocatalyst is the most important part of the photocatalytic technology. Therefore, the development of high-performance photocatalysts has attracted great attentions and many new photocatalysts such as oxides, sulfides, element, and polymers semiconductor photocatalysts were studied.

Recently, BiOX ($X = \text{Cl}, \text{Br}, \text{I}$) photocatalysts have been widely studied for their outstanding optical, electrical and catalytic properties. BiOX ($X = \text{Cl}, \text{Br}, \text{I}$) are a new inorganic graphene type photocatalysts which exhibit excellent photocatalytic activities and has attracted much attention all over the world due to their unique layer structures and appropriate band gaps [12–23]. Among all the

BiOX samples, BiOCl displays the best photocatalytic activity under UV light irradiation. For instance, Zhang and co-workers reported BiOCl exhibited better performance than TiO_2 (P25, Degussa) on photocatalytic degradation of methyl orange (MO) [24]. However, BiOCl can not show high photocatalytic reduction activity caused by the lower position conduction band minimum (CBM) as well as can not be excited under visible light irradiation. DFT calculations indicated that the position of CBM is mainly determined by the Bi 6p of BiOCl . This suggested that an effective way to regulate the CBM position of BiOX is adjustment content of bismuth. For example, Huang found that the increments of the content of bismuth in bismuth titanate $\text{Bi}_x\text{Ti}_y\text{O}_z$ can improve the position of CBM [25]. It indicates that the bismuth-rich strategy is feasible to improve the position of CBM and thus enhancing the photocatalytic reduction activity for $\text{Bi}_x\text{O}_y\text{X}_z$ ($X = \text{Cl}, \text{Br}, \text{I}$) photocatalysts. For instances, by bismuth-rich strategy, $\text{Bi}_{24}\text{O}_{31}\text{Br}_{10}$ displayed high photocatalytic activity the Cr(VI) reduction and H_2 production from water [26]. $\text{Bi}_{24}\text{O}_{31}\text{Cl}_{10}$ was synthesized by electrolytic corrosion of metal Bi, or calcination precursor, and it also showed high photocatalytic activity [27,28]. However, to the best of our knowledge, there are no reports about hydrothermal synthesis and photocatalytic molecular oxygen activation of $\text{Bi}_{24}\text{O}_{31}\text{Cl}_{10}$.

Molecular oxygen (O_2) is the most inexpensive and green oxidant for oxidation reaction. Unfortunately, because of spin forbidden reactions, O_2 cannot oxidize degrade most organic

* Corresponding authors at: Nanyang Normal University, College of Chemistry and Pharmaceutical Engineering, Nanyang 473061, China. Tel.: +86 0377 63513540.
E-mail addresses: yeliqun@163.com (L. Ye), Xie-hq@163.com (H. Xie).

pollutants under ambient conditions [29]. Therefore, we all know that the reactive oxygen species (ROS, such as $O_2^{\bullet-}$, H_2O_2 , and $\bullet OH$) are suggested as the main reactive species for photocatalytic degradation of pollutants. In photocatalytic process, molecular oxygen activation is occurred when photogenerated electrons on the surface of semiconductors reacting with O_2 to produce $O_2^{\bullet-}$ via one-electron reduction process, and then the $O_2^{\bullet-}$ can be reduced to $\bullet OH$ via two-electron reduction process [30,31]. So, it is very important to enhance the photocatalytic activity for molecular oxygen activation. In this work, via bismuth-rich strategy, $Bi_{24}O_{31}Cl_{10}$ nanosheets with $\{100\}$ facets exposure were synthesized, and its photocatalytic activity for molecular oxygen activation also were studied. The results showed that $Bi_{24}O_{31}Cl_{10}$ activated molecular oxygen to generate $O_2^{\bullet-}$ under visible light ($\lambda > 420$ nm) irradiation, and generate hydroxyl radical ($\bullet OH$) under UV–vis light irradiation.

2. Experimental

2.1. Materials and preparation

$Bi(NO_3)_3 \cdot 5H_2O$, NaCl, Nitroblue tetrazolium (NBT), and ammonia solution (NH_3 , 25–28%) were obtained from Sinopharm Chemical Reagent Co., Ltd. Ethanol were brought from Tianjin Kermel Chemical Reagent Co., Ltd. All the reagents we used were analytically pure without further purification.

For the syntheses of $Bi_{24}O_{31}Cl_{10}$ nanosheets, 0.004 mol of $Bi(NO_3)_3 \cdot 5H_2O$ and 0.004 mol of NaCl were dissolved in 24 mL of distilled water at room temperature with continuous stirring, and then ammonia solution was added dropwise to adjust the pH value of the solution to 10.3. The resulting solution were transferred into a 50 mL Teflon-lined stainless steel autoclave filled up to 80% of the total volume followed by a hydrothermal treatment at $160^\circ C$ for 18.5 h. After the reaction, the precipitate was collected, washed with deionized water and ethanol several times and dried at $60^\circ C$ in air. For comparison, BiOCl was obtained by using the same procedure without adding $NH_3 \cdot H_2O$.

2.2. Characterization

The crystalline phase of the samples was characterized by X-ray diffraction (XRD) by a Bruker D8 advance X-ray diffractometer at room temperature with Cu-K α radiation ($\lambda = 0.15418$ nm) and the 2θ ranging from 5° to 80° . Their size and morphology were inspected with scanning electron microscope (SEM, FEI, QUANTA 200). Transmission electron microscopy (TEM) and selected area electron diffraction (SAED) pattern and high-resolution transmission electron microscopy (HRTEM) image was obtained by a JEOL JEM-2100 (RH) with operating at an accelerating voltage of 200 kV. X-ray photoelectron spectroscopy (XPS) measurements were carried out by a VG Multilab 2000 spectrometer (Thermo Electron Corporation) with an Ar K α X-ray source. UV–vis diffuse reflectance spectra (DRS) were obtained using a Shimadzu UV-3600 spectrometer by using $BaSO_4$ as a reference. Photoluminescence (PL) spectra of the samples were recorded on a Fluorescence Spectrophotometer (Varian, CARY Eclipse).

2.3. Photocatalytic properties for molecular oxygen activation

The photocatalytic activities were evaluated under visible light ($\lambda > 420$ nm) or UV–vis light irradiation. The light was emitted by a 500 W high pressure xenon lamp (Changzhou Yuyu Electro-optical Device Co., Ltd. China). The visible light was obtained with a 420 nm cut-off filter using. Typical photocatalytic process is arranged in this way: 100 mL aqueous suspension of substrate (NBT (1.25×10^{-5} mol/L) solution; TA (5×10^{-4} mol/L) and NaOH (2×10^{-3} mol/L) solution) were placed in a beaker, and then 20 mg

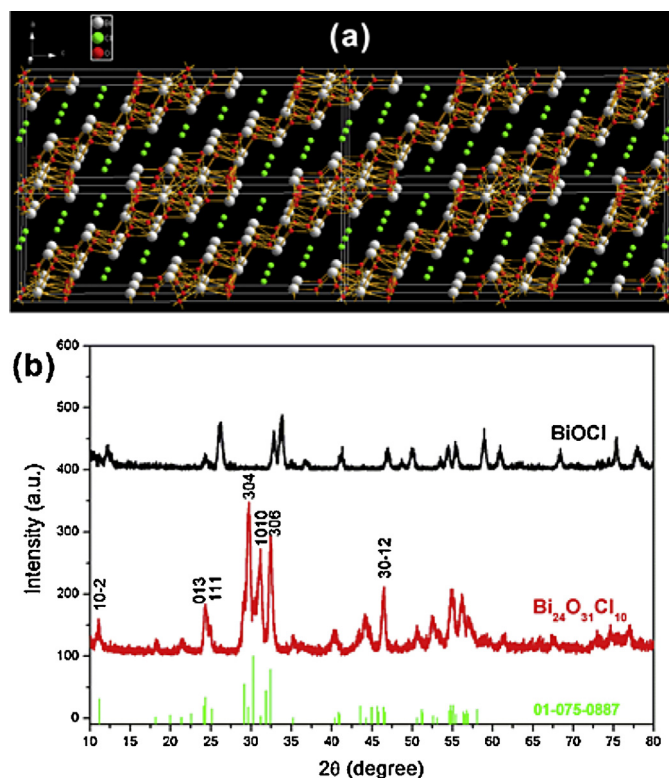


Fig. 1. (a) Schematic diagram of crystal structure of $Bi_{24}O_{31}Cl_{10}$, and (b) XRD patterns of as-prepared $Bi_{24}O_{31}Cl_{10}$ and BiOCl.

photocatalysts were added. Prior to irradiation, the suspensions were sonicated for 20 min and then were continuously stirred in dark for 30 min to reach adsorption-desorption equilibrium. The suspensions were kept under constant air-equilibrated conditions during irradiation. A magnetic stirrer was employed for continuous mixing. At the given time intervals, 6 mL suspensions were sampled, centrifuged, filtered and measured every 20 min. The upper clear liquid of TA–NaOH solution was analyzed by recording by PL spectra (Varian, CARY Eclipse) with $\lambda_{exc} = 315$ nm. The NBT solution was detected with UV–vis spectra (Perkin Elmer, Lambda 650s).

2.4. Electrochemical measurements

The Mott–Schottky curves were collected with an electrochemical analyzer (CHI660D, CHI Shanghai, Inc.) in a standard three electrode system. The $Bi_{24}O_{31}Cl_{10}$ photoanode (1×1 cm 2), platinum plate, saturated calomel electrode (SCE), and saturated KCl solution were used as working, counter, reference electrodes, and electrolyte, respectively. The working electrode was prepared via the dip-coating method. The Mott–Schottky measurements were monitored with independence-potential model to evaluate the band positions of $Bi_{24}O_{31}Cl_{10}$. And they were monitored at a fixed frequency of 100 Hz with 10 mV amplitude at various potentials.

3. Results and discussion

3.1. Catalyst characterization

Fig. 1a shows the schematic diagram of crystal structure of $Bi_{24}O_{31}Cl_{10}$. And Fig. 1b displays the XRD patterns of as-prepared $Bi_{24}O_{31}Cl_{10}$ and BiOCl nanosheets prepared by hydrothermal process, respectively. XRD analysis of the samples showed that they were both well crystallized. They can well be indexed to the hexagonal structures of BiOCl (JCPDS File No. 73-20600), and monoclinic

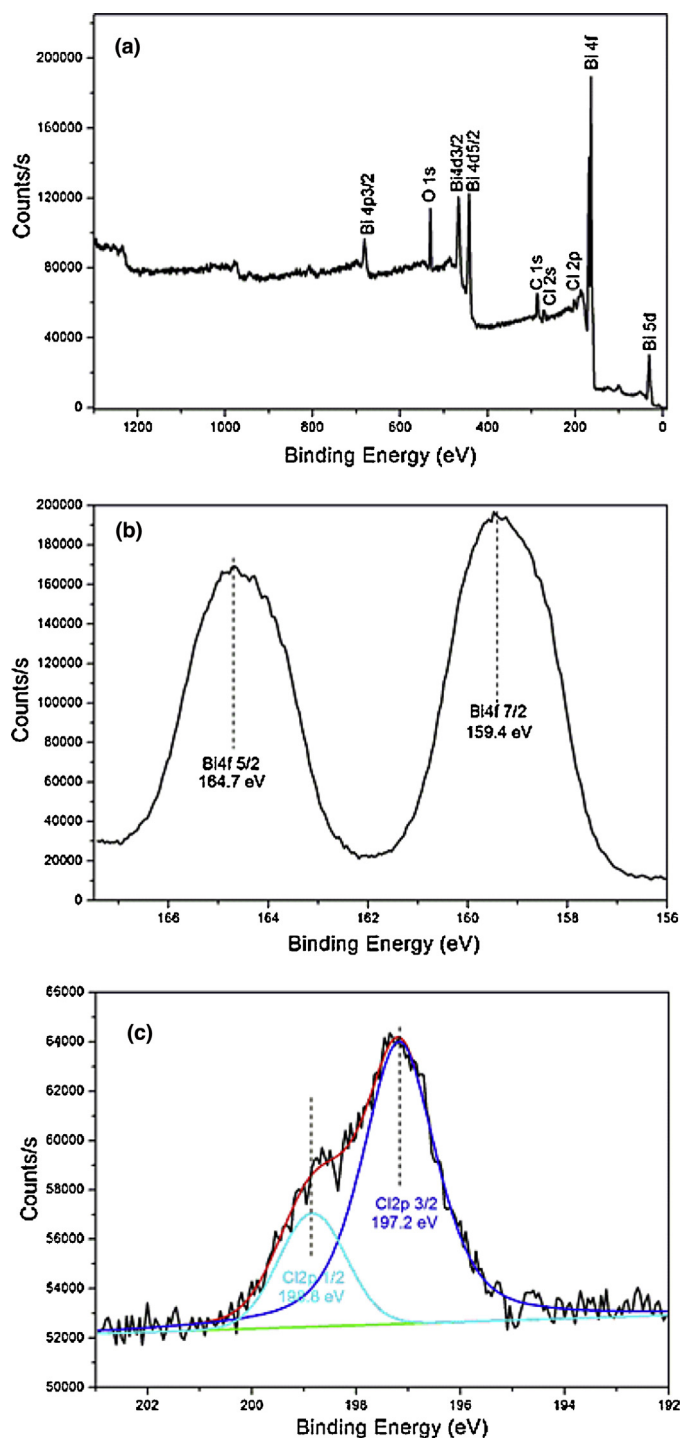


Fig. 2. Survey XPS spectrum (a) and high-resolution XPS spectra of $\text{Bi}_{24}\text{O}_{31}\text{Cl}_{10}$: Bi 4f (b) and Cl 2p (c).

$\text{Bi}_{24}\text{O}_{31}\text{Cl}_{10}$ (JCPDS File No. 01-075-0887), respectively [27,28]. On the other hand, no peaks of impurity (such as Bi_2O_3 and $\text{Bi}_3\text{O}_4\text{Cl}$) were detected in the above two samples. It indicates that both samples are pure.

The results of XPS spectrum of $\text{Bi}_{24}\text{O}_{31}\text{Cl}_{10}$ nanosheets (Fig. 2) also reveals that the product is consisted of Bi, O, Cl elements, and the atomic ratio of Bi/Cl was 2.5:1 within the experimental error. Fig. 2(b) and (c) show the high-resolution XPS spectra of Bi 4f and Cl 2p, respectively. The two peaks of the Bi region at 164.7 and 159.4 eV are assigned to Bi 4f 5/2 and Bi 4f 7/2. They are related to Bi^{3+} in Bi–O band in $\text{Bi}_{24}\text{O}_{31}\text{Cl}_{10}$ nanostructure [26]. The Cl 2p

region can be deconvoluted into two peaks at 198.8 and 197.2 eV as shown in Fig. 2(c), corresponding to Cl 2p1/2 and Cl 2p3/2. Based on the XRD and XPS results, it can be concluded that the as-synthesized sample was $\text{Bi}_{24}\text{O}_{31}\text{Cl}_{10}$.

The morphology of as-prepared BiOCl and $\text{Bi}_{24}\text{O}_{31}\text{Cl}_{10}$ were characterized as shown in Fig. 3 and Fig S1. Fig. 3(a) and (b) displays that BiOCl sample. They showed that BiOCl is mainly consisted of irregular nanoplates, which are 1–3 μm in width and ca. 300 nm in thickness. While $\text{Bi}_{24}\text{O}_{31}\text{Cl}_{10}$ were consists of quantity of nanosheets with ca. 5 μm in width and about 10–30 nm in thickness (Fig. 3a and b and Fig S1). To our best knowledge, this is the first time to have synthesized $\text{Bi}_{24}\text{O}_{31}\text{Cl}_{10}$ photocatalytic material with such a large ratio between the surface and thickness.

Fig. 4(a) shows the transmission electron microscopy (TEM) image of $\text{Bi}_{24}\text{O}_{31}\text{Cl}_{10}$ nanosheets. It can be found that the as-synthesized $\text{Bi}_{24}\text{O}_{31}\text{Cl}_{10}$ nanosheets are thin and the corresponding SAED pattern (Fig. 4(b)) displayed diffraction spots of (0 1 7), (0 2 0) and (0 1 –7). And angles of (0 1 7)–(0 2 0) and (0 1 –7)–(0 2 0) were 43.6 and 44.6°, respectively, which are consistent with the theoretical interfacial angles between {0 1 7} and {0 2 0} facets (43.6°) and between {0 1 –1} and {0 2 0} facets (44.6°). It proved that the main exposed facets of $\text{Bi}_{24}\text{O}_{31}\text{Cl}_{10}$ nanosheets are {1 0 0} facets. For checking the result again, the HRTEM and FFT images $\text{Bi}_{24}\text{O}_{31}\text{Cl}_{10}$ nanosheets are shown in Fig. 4(c) and (d). The HRTEM image of a single $\text{Bi}_{24}\text{O}_{31}\text{Cl}_{10}$ crystal (viewed from the [1 0 0] axis) shows two different distinct lattice fringes of 0.273 nm and 0.278 nm, which are in good agreement with the crystallographic planes of (0 1 –7) and (0 1 7) in $\text{Bi}_{24}\text{O}_{31}\text{Cl}_{10}$ with monoclinic phase, respectively. The angle of (0 1 7) and (0 1 –7) was 88.4, respectively, which are consistent with the theoretical interfacial angle ($b=88.7^\circ$). Fig. 4(d) was the corresponding FFT pattern. It displayed that angles of (0 1 7)–(0 2 0) and (0 1 –7)–(0 2 0) were 43.6 and 44.7°, respectively, which also are consistent with the theoretical interfacial angle. Both HRTEM and FFT images show the $\text{Bi}_{24}\text{O}_{31}\text{Cl}_{10}$ nanosheets are single crystals with {1 0 0} facets exposure.

Fig. 5(a) shows the UV–vis diffuse absorption spectra of BiOCl and $\text{Bi}_{24}\text{O}_{31}\text{Cl}_{10}$ nanosheets. It can be seen that BiOCl has almost no absorption in the visible light region with an absorption edge at about 364 nm, whereas $\text{Bi}_{24}\text{O}_{31}\text{Cl}_{10}$ has strong absorption in the visible light region with an absorption edge about 460 nm. These results are consistent with the white and light yellow colors of BiOCl and $\text{Bi}_{24}\text{O}_{31}\text{Cl}_{10}$ nanosheets, respectively. The band gap energy of a semiconductor can be evaluated by the following equation [15,32]:

$$\alpha h\nu = A(h\nu - E_g)^{n/2} \quad (1)$$

where α , h , ν , A , and E_g represent the absorption coefficient, Planck's constant, light frequency, energy-independent constant, and band gap, respectively. The value of n depends on the characteristics of the transition, including direct transition ($n=1$) and indirect transition ($n=4$). For bismuth-based photocatalysts, n is 4 for their indirect transition [33]. The band gap energies (E_g values) of $\text{Bi}_{24}\text{O}_{31}\text{Cl}_{10}$ can be thus estimated from a plot of $(\alpha h\nu)^{1/2}$ versus photo energy ($h\nu$), which is shown in Fig. 5(b). The estimated band gap energies of the resulting samples were about 3.42 and 2.71 eV for BiOCl and $\text{Bi}_{24}\text{O}_{31}\text{Cl}_{10}$, respectively.

3.2. Photocatalytic activity

Molecular oxygen activation is extremely important for photocatalytic degradation of organic pollutants. It not only inhibits the recombination of photogenerated electron-hole pairs but also produces reactive oxygen species (ROS), such as $\text{O}_2^{\bullet-}$, and $\bullet\text{OH}$ [34–36]. In this work, nitroblue tetrazolium (NBT) was chosen to quantize the $\text{O}_2^{\bullet-}$ and demonstrate the photocatalytic activity for molecular oxygen activation via one-electron reduction process.

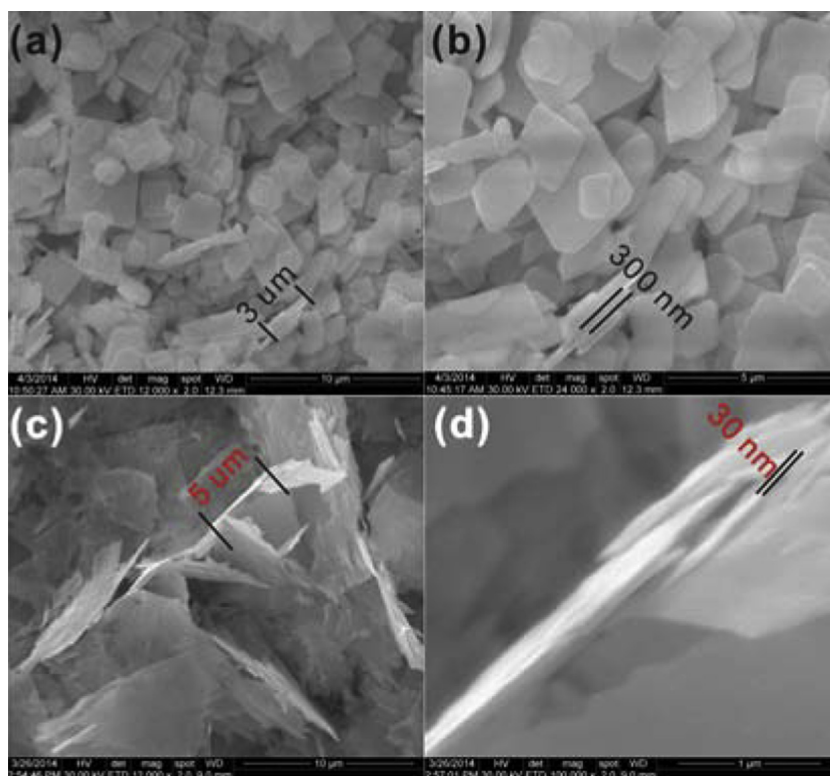


Fig. 3. Low-(a) and high-(b) magnification SEM images of as-prepared BiOCl sample, and low-(c) and high-(d) magnification SEM images of as-prepared Bi₂₄O₃₁Cl₁₀ nanosheets.

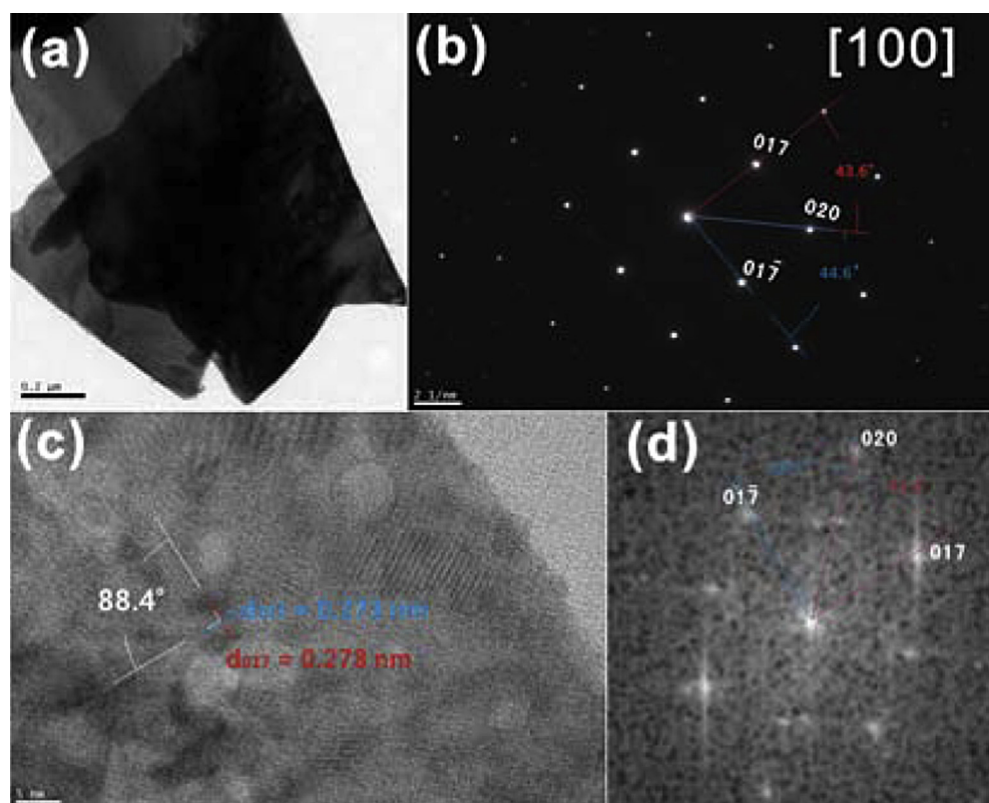


Fig. 4. TEM image (a), SAED pattern (b), HRTEM image (c), and its FFT pattern (d) of Bi₂₄O₃₁Cl₁₀ nanosheets.

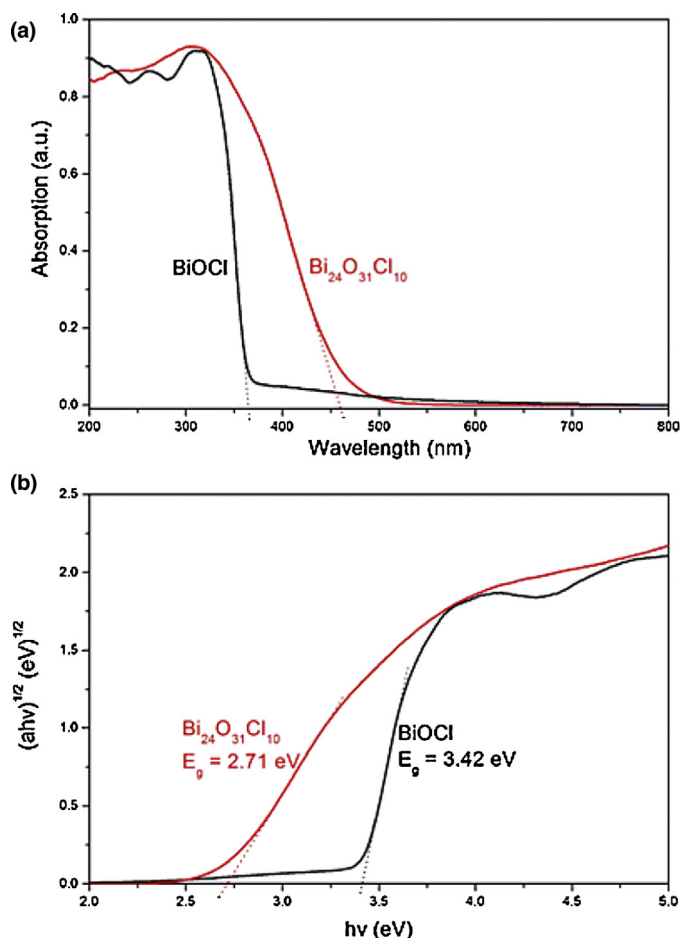


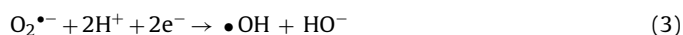
Fig. 5. DRS and plots of $(\alpha hv)^{1/2}$ vs. photon energy ($h\nu$) for the as-prepared BiOCl nanoplates and Bi₂₄O₃₁Cl₁₀ nanosheets.

Fig. S2 shows the UV–vis absorption spectra of the suspensions of Bi₂₄O₃₁Cl₁₀ and BiOCl under visible light irradiation. It is obvious that the maximum absorbance in the UV–vis spectra of NBT declines with the irradiation time increasing. It indicated that photogenerated electron can react with O₂ to produce O₂^{•−} (Eq. (2)) in the Bi₂₄O₃₁Cl₁₀ suspension under visible light irradiation (Fig. 6).

However, there are no changes in the UV–vis spectra of NBT in the BiOCl suspension, which implies no O₂^{•−} generation.



Hydroxyl radical (•OH) is another important product of molecular oxygen activation. From the theoretical viewpoint, it is almost impossible for the production of •OH in the bismuth-based photocatalysts system via photocatalytic oxidation of H₂O, because of the standard redox potential of Bi⁺⁵/Bi⁺³ (+1.59 V) is more negative than that of •OH/−OH (+1.99 V) [15,37]. So, the •OH should be produced via two-electron reduction by activating molecular oxygen for Bi-based photocatalysts (Eq. (3)). TA can react with •OH to generate fluorescence TAOH. As shown in Fig. 6 and Fig. S3, it can be seen that nearly no •OH generation from both Bi₂₄O₃₁Cl₁₀ and BiOCl in TA solutions during the visible light irradiation. It indicated that •OH cannot generate via two-electron reduction for Bi₂₄O₃₁Cl₁₀ and BiOCl under visible light irradiation.



Considering that BiOCl cannot be excited by visible light, the photocatalytic molecular oxygen activation activity for Bi₂₄O₃₁Cl₁₀ and BiOCl also was compared under UV–vis light irradiation.

Fig. 7 Figs. S4 and S5 showed the photocatalytic activity for molecular oxygen activation via one-electron reduction process to produce O₂^{•−} and two-electron reduction process to produce •OH from O₂^{•−}, respectively. It can be seen that the UV–vis light results were very different with visible light induced results. For, BiOCl, it showed high photocatalytic activity for molecular oxygen activation via one-electron reduction process to produce O₂^{•−}. But BiOCl cannot active molecular oxygen via two-electron reduction process to produce •OH. For Bi₂₄O₃₁Cl₁₀, it showed higher photocatalytic activity for molecular oxygen activation via one-electron reduction process to produce O₂^{•−} than that of visible light induced results. More surprisingly, •OH was generated under UV–vis light irradiation for Bi₂₄O₃₁Cl₁₀.

3.3. Reason analysis

To further elucidate the electronic structure of Bi₂₄O₃₁Cl₁₀ and BiOCl, electrochemical flat potential measurements were carried out, and the data were plotted in Mott–Schottky coordinates, as

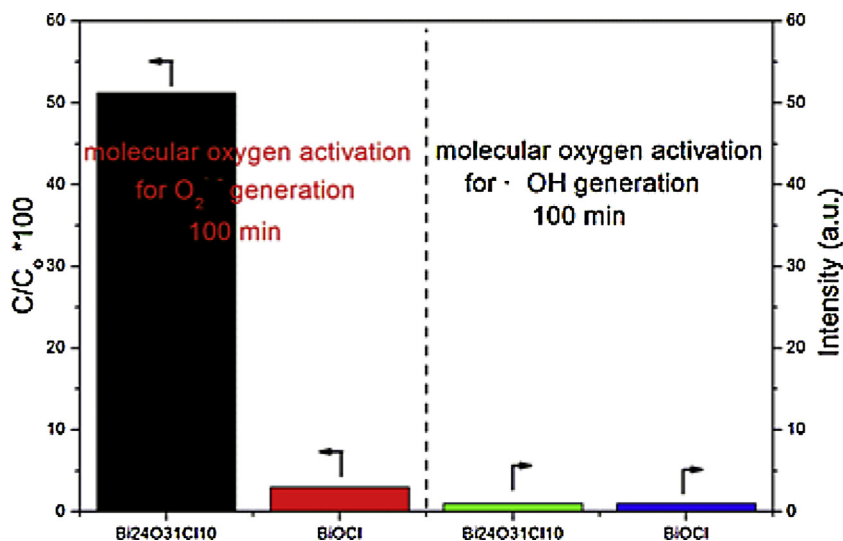


Fig. 6. Photocatalytic molecular oxygen activation activity for O₂^{•−} and •OH generation by Bi₂₄O₃₁Cl₁₀ and BiOCl under visible light irradiation.

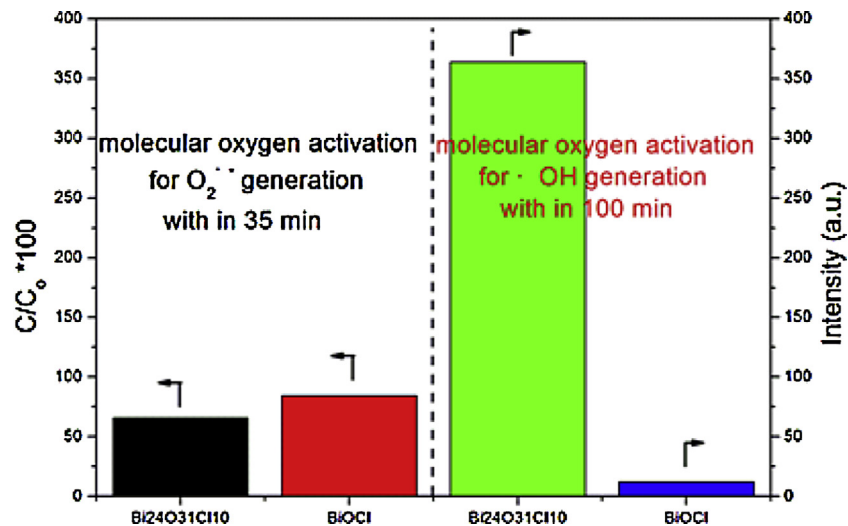


Fig. 7. Photocatalytic molecular oxygen activation activity for $O_2^{\bullet-}$ and $\bullet OH$ generation by $Bi_{24}O_{31}Cl_{10}$ and $BiOCl$ under UV–vis light irradiation.

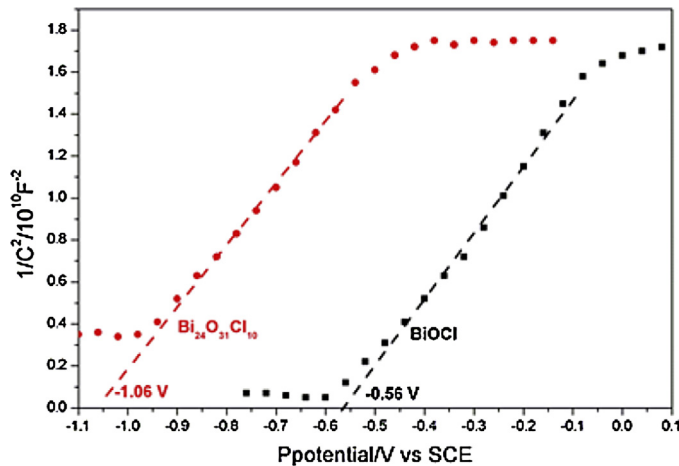


Fig. 8. Mott–Schottky plot for $Bi_{24}O_{31}Cl_{10}$ and $BiOCl$ electrode in saturated KCl solution vs SCE.

shown in Fig. 8. Generally, flat-band potential values are determined using the following equation:

$$\frac{1}{C^2} = \frac{2(E - E_{fb} - K_B T/q)}{(\epsilon \epsilon_0 N_D)} \quad (4)$$

where C is the space charge capacitance, N_D is the donor density, ϵ and ϵ_0 are the dielectric constants of free space and the film electrode, respectively, E is the applied potential, E_{fb} is the flat-band potential, K_B is Boltzmann's constant, T is the temperature, and q is the electronic charge. For $Bi_{24}O_{31}Cl_{10}$, the flat potential obtained by the extrapolation of the Mott–Schottky plot is roughly -1.06 V versus the saturated calomel electrode (SCE), which is equivalent to -0.82 V versus the normal hydrogen electrode (NHE). It is known that the conduction bands of n-type semiconductors are about 0.1 V higher than flat potentials, depending on the electron effective mass and carrier concentration [38–40]. So, the bottom of the conduction band (CBM) of $Bi_{24}O_{31}Cl_{10}$ is -0.91 V. The reduction potential of $O_2/O_2^{\bullet-}$ is -0.28 V (NHE). The negative value of the flat-potential clearly indicates that $Bi_{24}O_{31}Cl_{10}$ can effectively active molecular oxygen to generate $O_2^{\bullet-}$. And the high concentration $O_2^{\bullet-}$ of $Bi_{24}O_{31}Cl_{10}$ resulted in more $\bullet OH$ generation due to the Le Chatelier's principle (Eq. (4)). For $BiOCl$, the CBM is

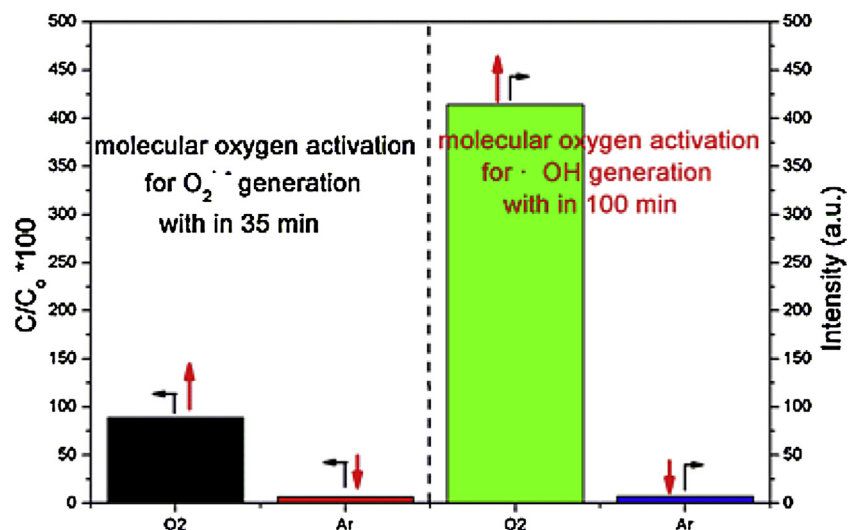


Fig. 9. Oxygen-control experiment for photocatalytic molecular oxygen activation activity by $Bi_{24}O_{31}Cl_{10}$ under UV–vis light irradiation.

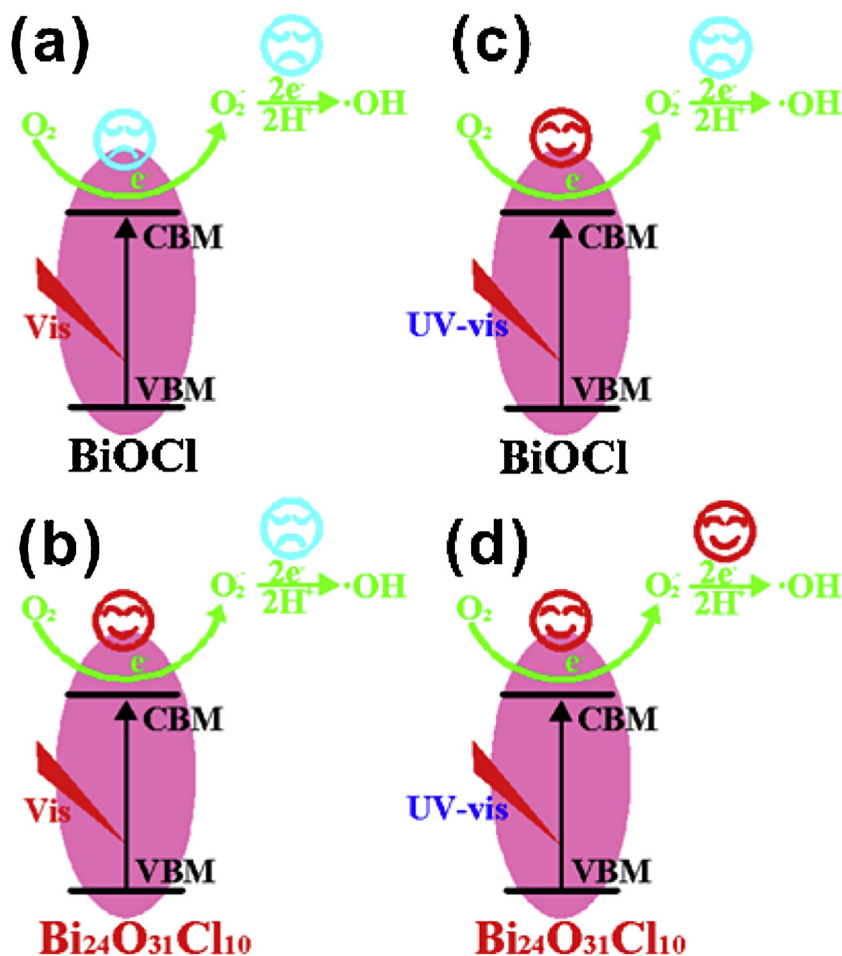


Fig. 10. The possible activation way of molecular oxygen over $Bi_{24}O_{31}Cl_{10}$ and BiOCl. $Bi_{24}O_{31}Cl_{10}$ can effectively activate molecular oxygen to generate superoxide radical ($O_2^{\bullet-}$) under visible light ($\lambda > 420$ nm) irradiation, and generate $O_2^{\bullet-}$ and hydroxyl radical ($\cdot OH$) under UV-vis light irradiation.

confirmed about -0.41 V (NHE). So, it also can activate O_2 to produce $O_2^{\bullet-}$ via single electron oxygen reduction. And the CBM potential of BiOCl is enough for the two-electron oxygen reduction to generate $\cdot OH$ from $O_2^{\bullet-}$ (Eq. (4)). But, comparing with the CBM $Bi_{24}O_{31}Cl_{10}$ (-0.91 V), the photocatalytic reduction activity of BiOCl for $O_2^{\bullet-}$ generation should be lower than $Bi_{24}O_{31}Cl_{10}$. Therefore, due to the Le Chatelier's principle, the low concentration $O_2^{\bullet-}$ of BiOCl result in fewer $\cdot OH$ generation. On the other hand, the percent conversion of Eq. (4) may be different for $Bi_{24}O_{31}Cl_{10}$ and BiOCl. The more $\cdot OH$ generation of $Bi_{24}O_{31}Cl_{10}$ also may be due to its higher percent conversion for Eq. (2). And the data presented in Fig. 7 can support this point. A large number of $O_2^{\bullet-}$ was converted to $\cdot OH$ for $Bi_{24}O_{31}Cl_{10}$, but few $O_2^{\bullet-}$ was converted for BiOCl. And so, the amount of $O_2^{\bullet-}$ of $Bi_{24}O_{31}Cl_{10}$ is lesser than BiOCl under UV-vis light.

The controlled experiment was used to further demonstrate the origin of $O_2^{\bullet-}$ and $\cdot OH$ under UV-vis light irradiation. As shown in Fig. 9, the generated quantum of $O_2^{\bullet-}$ or $\cdot OH$ are enhanced with O_2 blowing. However, the generated quantum of $O_2^{\bullet-}$ or $\cdot OH$ are negligible with Ar blowing. It indicates that the origin of $O_2^{\bullet-}$ and $\cdot OH$ are O_2 . Based on the above photocatalytic results and MS analysis, the possible activation way of molecular oxygen over BiOCl and $Bi_{24}O_{31}Cl_{10}$ are proposed in Fig. 10.

Under visible light irradiation, BiOCl cannot be excited (Fig. 10a). So, BiOCl can't active molecular oxygen to produce ROS. However, $Bi_{24}O_{31}Cl_{10}$ displayed absorption under visible range. Therefore, it showed photocatalytic activity for molecular oxygen activation to produce $O_2^{\bullet-}$ (Fig. 10b). But, due to the low energy of visible light,

$Bi_{24}O_{31}Cl_{10}$ cannot activate molecular oxygen to generate much $O_2^{\bullet-}$. Therefore, There are no $\cdot OH$ generation via two-electron reduction process from $O_2^{\bullet-}$ due to the Le Chatelier's principle. Under UV-vis light irradiation, BiOCl can be excited. It showed photocatalytic molecular oxygen activation activity to produce $O_2^{\bullet-}$. But, the low CBM potential of BiOCl results in low photocatalytic reduction activity and little $O_2^{\bullet-}$ generation, and no $\cdot OH$ generation via two-electron reduction process from $O_2^{\bullet-}$ due to the Le Chatelier's principle (Fig. 10c). For $Bi_{24}O_{31}Cl_{10}$, the high energy of UV light and high CBM potential results in much $O_2^{\bullet-}$ generation and high photocatalytic reduction activity, respectively. Therefore, $\cdot OH$ generation via two-electron reduction process from $O_2^{\bullet-}$ (Fig. 10d).

4. Conclusions

In summary, two-dimensional $Bi_{24}O_{31}Cl_{10}$ single-crystalline nanosheets with $\{100\}$ facet exposure was synthesized and characterized by XRD, XPS, SAED, SEM, TEM, HRTEM and DRS. The size of a single nanosheet is about $5 \mu m$ in width and $10\text{--}30$ nm in thickness, which results in a large ratio of surface to thickness and higher exposure ratio of $\{100\}$ facets. To our knowledge, this is the first report on synthesis of $Bi_{24}O_{31}Cl_{10}$ with such a large ratio of surface to thickness. Compared to BiOCl, $Bi_{24}O_{31}Cl_{10}$ can absorb more visible light and showed effectively activate molecular oxygen to generate $O_2^{\bullet-}$ under visible light ($\lambda > 420$ nm) irradiation. In addition, $Bi_{24}O_{31}Cl_{10}$ can activate molecular oxygen to generate $\cdot OH$ via two-electron reduction under UV-vis light irradiation. The CBM of

$\text{Bi}_{24}\text{O}_{31}\text{Cl}_{10}$ is calculated to be -0.91 V , indicating that $\text{Bi}_{24}\text{O}_{31}\text{Cl}_{10}$ may produce H_2 from water under visible light irradiation.

Acknowledgments

This work was supported by the Henan Joint Funds of the National Natural Science Foundation of China (No. U1404506), the Natural Science Foundation of Henan Department of Science & Technology (No. 142102210477), Natural Science Foundation of Henan Department of Education (No. 14A150021) and the Natural Science Foundation of Nanyang Normal University (No. ZX2014039).

Appendix A. Supplementary data

Supplementary material related to this article can be found, in the online version, at <http://dx.doi.org/10.1016/j.apcatb.2014.10.075>.

References

- [1] A.L. Linsebigler, G. Lu, J.T. Yates, *Chem. Rev.* 95 (1995) 735–758.
- [2] J.H. Carey, J. Lawrence, H.M. Tosine, *Bull. Environ. Contam. Toxicol.* 16 (1976) 697–701.
- [3] A. Mills, R.H. Davies, D. Worsley, *Chem. Soc. Rev.* 22 (1993) 417–425.
- [4] O. Legrini, A.M. Braun, E. Oliveros, *Chem. Rev.* 93 (1993) 671–698.
- [5] M.R. Hoffmann, S.T. Martin, W. Choi, D.W. Bahnemann, *Chem. Rev.* 95 (1995) 69–96.
- [6] A. Heller, *Acc. Chem. Res.* 28 (1995) 503–508.
- [7] Z.G. Zou, J.H. Ye, K. Sayama, H. Arakawa, *Nature* 414 (2001) 625–627.
- [8] A. Kudo, Y. Misaki, *Chem. Soc. Rev.* 38 (2009) 253–278.
- [9] F.E. Osterloh, *Chem. Mater.* 20 (2008) 35–54.
- [10] T. Ione, A. Fujishima, S. Konishi, K. Honda, *Nature* 277 (1979) 637–638.
- [11] Q. Liu, Y. Zhou, J. Kou, X. Chen, Z. Tian, J. Gao, S. Yan, Z.J. Zou, *Am. Chem. Soc.* 132 (2010) 14385–14387.
- [12] X. Zhang, Z. Ai, F. Jia, L. Zhang, *J. Phys. Chem. C* 112 (2008) 747–753.
- [13] J. Henle, P. Simon, A. Frenzel, S. Scholz, S. Kaskel, *Chem. Mater.* 19 (2007) 366–373.
- [14] M.A. Gondala, X. Chang, M.A. Ali, Z.H. Yaman, Q. Zhou, G. Ji, *Appl. Catal., A: Gen.* 397 (2011) 192–200.
- [15] L. Ye, J. Liu, C. Gong, L. Tian, T. Peng, L. Zan, *ACS Catal.* 2 (2012) 1677–1683.
- [16] L. Ye, C. Gong, J. Liu, L. Tian, T. Peng, K. Deng, L. Zan, *J. Mater. Chem.* 22 (2012) 8354–8360.
- [17] Y.F. Fang, W.H. Ma, Y.P. Huang, G.W. Cheng, *Chem. Eur. J.* 19 (2013) 3224–3229.
- [18] Y. Feng, L. Li, J. Li, J. Wang, L. Liu, *J. Hazard. Mater.* 192 (2011) 538–544.
- [19] Y. Fan, Y. Huang, J. Yang, P. Wang, G. Cheng, *Environ. Sci. Technol.* 45 (2011) 1593–1600.
- [20] J. Xu, W. Meng, Y. Zhang, L. Li, C. Guo, *Appl. Catal., B: Environ.* 107 (2011) 355–362.
- [21] X. Xiao, R. Hao, M. Liang, X.X. Zuo, J.M. Nan, L.S. Li, W.D. Zhang, *J. Hazard. Mater.* 233–234 (2012) 122–130.
- [22] F. Dong, Y.J. Sun, M. Fu, Z.B. Wu, S.C. Lee, *J. Hazard. Mater.* 219–220 (2012) 26–34.
- [23] J. Cao, B.Y. Xu, H.L. Lin, B.D. Luo, S.F. Chen, *Catal. Commun.* 26 (2012) 204–208.
- [24] K.L. Zhang, C.M. Liu, F.Q. Huang, W.D. Wang, *Appl. Catal., B: Environ.* 68 (2006) 125–130.
- [25] W. Wei, Y. Dai, B. Huang, *J. Phys. Chem. C* 113 (2009) 5658–5663.
- [26] J. Shang, W.C. Hao, X.J. Lv, T.M. Wang, X.L. Wang, Y. Du, S.X. Dou, T.F. Xie, D.J. Wang, J.O. Wang, *ACS Catal.* 4 (2014) 954–961.
- [27] F.T. Li, Q. Wang, X.J. Wang, B. Li, Y.J. Hao, R.H. Liua, D.S. Zhao, *Appl. Catal., B: Environ.* 150–151 (2014) 574–584.
- [28] G. Che, G.L. Fang, G.D. Tang, *Mater. Res. Bull.* 48 (2013) 1256–1261.
- [29] M. Metz, E.I. Solomon, *J. Am. Chem. Soc.* 123 (2001) 4938–4950.
- [30] Y.B. Zhao, W.H. Ma, Y. Li, H.W. Ji, C.C. Chen, H.Y. Zhu, J.C. Zhao, *Angew. Chem., Int. Ed.* 51 (2012) 3188–3192.
- [31] L. Khachatryan, E. Vejerano, S. Lomnicki, B. Dellinger, *Environ. Sci. Technol.* 45 (2011) 8559–8566.
- [32] T.B. Li, G. Chen, C. Zhou, Z.Y. Shen, R.C. Jin, J.X. Sun, *Dalton Trans.* 40 (2011) 6751–6758.
- [33] X. Xiao, R. Hao, M. Liang, X.X. Zuo, J.M. Nan, L.S. Li, W.D. Zhang, *J. Hazard. Mater.* 233–234 (2012) 122–130.
- [34] Y. Li, W. Zhang, J.F. Niu, Y.S. Chen, *ACS Nano* 6 (2012) 5164–5173.
- [35] M.A. Henderson, I. Lyubinetzky, *Chem. Rev.* 113 (2013) 4428–4455.
- [36] E. Wahlstrom, E.K. Vestergaard, R. Schaub, A. Ronnau, M. Vestergaard, E. Lagsgaard, I. Stensgaard, F. Besenbacher, *Science* 303 (2004) 511–513.
- [37] H. Fu, C. Pan, W. Yao, Y. Zhu, *J. Phys. Chem. B* 109 (2005) 22432–22439.
- [38] W.J. Luo, Z.S. Li, X.J. Jiang, T. Yu, L.F. Liu, X.Y. Chen, J.H. Ye, Z.G. Zou, *Phys. Chem. Chem. Phys.* 10 (2008) 6717–6723.
- [39] J.L. Wang, Y. Yu, L.Z. Zhang, *Appl. Catal., B: Environ.* 136–137 (2013) 112–121.
- [40] X.Y. Xiao, J. Jiang, L.Z. Zhang, *Appl. Catal., B: Environ.* 142–143 (2013) 487–493.